Acta Astronautica 198 (2022) 431–444

Contents lists available at ScienceDirect

Acta Astronautica

journal homepage: www.elsevier.com/locate/actaastro

Simplified analytical models for hypersonic lateral-directional stability

Shuai-Qi Guo [1], Wen Liu [*,2], Chen-An Zhang [3], Xiang Zhou [4], Fa-Min Wang [5]

State Key Laboratory of High Temperature Gas Dynamics, Chinese Academy of Sciences, 100190, Beijing, People's Republic of China

ARTICLE INFO

Keywords:
Lateral stability
Directional stability
Analytical model
Viscous effects

ABSTRACT

The balance of lateral and directional static stability plays an important role in the lateral-directional dynamics and vehicle design. The theory of geometric influence on the lateral and directional static stability is mature for conventional aircrafts. However, the distinct configuration characteristics and flow physics for hypersonic vehicles may lead to different design theory, which is absent now. In order to solve this problem, simplified analytical models of lateral-directional static derivatives are proposed based on the simplified geometry model. It's found that the lateral and directional stability both increase as the deflection angle, dihedral angle, or angle of attack increases, whereas the influence of sweep angle can be neglected. The difference lies in that the lateral stability is proportional to dihedral angle while the directional stability is proportional to the square of dihedral angle. The reasonable accuracy is validated in comparison with the inviscid numerical solutions. Furthermore, the influence mechanism of viscous effects on the lateral and directional stability is investigated in detail based on the numerical results. It's found that the strong viscous interaction can improve the lateral stability evidently, and both the strong viscous interaction and the shear stress can lead to the increase of the directional stability. In addition, the lateral stability is slightly reduced by the chemical nonequilibrium effects.

1. Introduction

Lateral and directional stability design is a critical issue for any kind of aircraft. For traditional aircrafts, the lateral stability can be easily improved by changing the wing geometric sweep and dihedral, as well as wing fuselage interface [1]. The directional stability is mainly dominated by the contribution of the vertical tail, which also influences the lateral stability. However, to alleviate the serious aerothermal heating of hypersonic vehicles, especially for long-time flight, the vertical tail is generally restrained in size strictly or even fully removed [2]. This would make the improvement of the directional stability rather difficult. Besides, in order to obtain high aerodynamic and structural efficiency, the configuration of hypersonic vehicles generally presents the feature that the wing and body being highly blended. The difference in configuration features and flow characteristics may make the stability design theory of hypersonic vehicles rather distinct from that of the conventional aircrafts. Cockrell et al. [3] have compared the aerodynamic performance of two waveriders with a straight and cranked wing, respectively, and found that the latter configuration has better lateral stability. Rasmussen [4] has further elaborated on the above results by analyzing two other configurations and found that waveriders with finlets or positive dihedral tend to be stable in rolling-sideslip modes. Pezzella [5] has compared the lateral-directional stability of different configurations for a small hypersonic flying test bed. Bykerk et al. [6] have conducted a detailed lateral-directional stability analysis of the HEXAFLY-INT hypersonic vehicle under subsonic flight conditions along with in-depth flowfield analysis. Shang et al. [7] have investigated the effects of elastic deformation on the rolling stability of the slender waverider vehicle. Aprovitola et al. [8] have developed a parametric model for the re-entry vehicle shape optimization, which can improve the lateral-directional stability by flexibly alter the characteristics of the winglet dihedral. Liu et al. [9] have conducted a parametric study on the lateral-directional stability of hypersonic waveriders and found that increasing the dihedral angle of the lower surface can improve not only the lateral static stability, but

* Corresponding author.
E-mail address: lw@imech.ac.cn (W. Liu).
[1] Master's Student, Institute of Mechanics.
[2] Assistant Professor, Institute of Mechanics.
[3] Professor, Institute of Mechanics.
[4] Master's Student, Institute of Mechanics.
[5] Professor, Institute of Mechanics.

https://doi.org/10.1016/j.actaastro.2022.06.024
Received 25 March 2022; Received in revised form 14 June 2022; Accepted 18 June 2022
Available online 21 June 2022

Nomenclature

b	total span of the geometry model, m
C_l, C_n, C_y	roll moment coefficient, yaw moment coefficient, and side force coefficient
$C_{l\beta}$	lateral static derivative, rad^{-1}
$C_{n\beta}$	directional static derivative, rad^{-1}
$C_{y\beta}$	side force static derivative, rad^{-1}
C_p	pressure coefficient
h	total height of the geometry model, m
L	total length of the geometry model, m
L_{ref}	reference length, $b/2$ for C_l and L for C_n
M_∞	freestream Mach number
P	static pressure, Pa
q_∞	freestream dynamic pressure, Pa
S_{half}	surface area of half model for the lower surface, m^2
S_{ref}	reference area, m^2, being equal to S_{half}
V	freestream velocity, m/s
x,y,z	spatial coordinates, m
$\overline{x}$	distance of centroid away from the nose along the X-axis, $2/3L$ for the simplified geometry model
$\overline{y}$	distance of centroid away from the nose along the Y-axis, $1/3\ b/2 = b/6$ for the simplified geometry model
$\overline{z}$	distance of centroid away from the nose along the Z-axis, $1/3h$ for the simplified geometry model
α	angle of attack
β	sideslip angle
θ	deflection angle
Γ	dihedral angle
Λ	sweep angle
ξ	mass faction of each species

also the directional static stability. However, further insight into the physics nature of the quantitative geometric influence on lateral-directional static stability still remains to be studied.

Similar to the conventional theory of flight dynamics [1,10,11], it is of vital interest to seek analytical methods that can directly construct the relationship between the geometric features and stability for hypersonic vehicles. Some efforts have been made to construct such analytical techniques. Mason [12] has introduced the derivation of the yaw moment contribution from the vertical tail using both supersonic linear theory and hypersonic Newtonian theory. It is found that the contribution to directional stability is proportional to the wedge angle at hypersonic speed, leading to the X-15 wedge vertical tail design with large base area. Jia et al. [13] have derived the analytical expression between the geometric features and the center of pressure by applying the Newtonian theory on a simplified streamline model, which indicates that the convex streamline is desirable to improve the longitudinal stability.

Gaining such understanding will definitely lead to better and more efficient vehicle designs. Therefore, this paper tries to develop simplified analytical models to provide guidance for hypersonic lateral-directional static stability design. To this end, a simplified geometry model is first introduced to be representative of the typical hypersonic lifting-body configuration. Then the Newtonian theory is applied to derive the analytical models of lateral-directional static derivatives with respect to the geometric parameters. And the accuracy is validated in contrast to the inviscid Computational-Fluid-Dynamics (CFD) solutions. Finally, the influence mechanism of viscous effects is analyzed in detail based on the CFD results, including the laminar flow, turbulent flow, and chemical nonequilibrium effects.

2. Model derivation

Tarpley et al. [14] have presented an efficient and high-fidelity calculation method of stability derivatives for the simple caret-wing waveriders by using the linear piston theory. However, the expressions are too complex to analyze the direct relationship between the main geometric features and the stability. Therefore, in order to capture the dominant influence of geometric features, such as the results introduced in Ref. [12], a simplified geometry model is presented and then the Newtonian theory is employed to derive analytical expressions of lateral-directional static derivatives with simple form.

Considering the fact that the upper surface generally has a minor influence on the total aerodynamic performance of typical hypersonic vehicles with high lift-to-drag ratio at positive angles of attack, especially the waverider [9], the discussion is limited only to the lower surface in this paper.

2.1. Simplified geometry model

Simplified geometry model being ease of parametric description is quite favorable for analytical derivations. A lifting-body model with delta planform is used here for lateral-directional stability analysis, which can be deemed an extreme simplification of the cone-derived waverider. As sketched in Fig. 1, the configuration has constant sweep angle Λ along the leading edge, constant dihedral angle Γ in the Y-Z cross section, and constant deflection angle θ in the X-Z cross section. The upper surface is parallel to the freestream. When the length is given, the shape can be specified by only two independent parameters: deflection angle θ and dihedral angle Γ. The sweep angle can be determined according to the geometric relationship as follows

$$\tan\Lambda = \frac{\tan\Gamma}{\tan\theta} \tag{1}$$

2.2. Lateral static derivative $C_{l\beta}$

According to the theory of traditional flight dynamics, for a swept-back wing, positive sideslip produces an increase in effective speed and a decrease in effective angle of attack on the right semispan (Y > 0). The case is just opposite for the left semispan (Y < 0). The change in effective speed, shown in Fig. 2, plays a dominant role, making the lift of the right semispan turns larger than that of the left semispan. Therefore, increasing the sweep angle can improve the lateral static stability. The effective speed can be expressed as follows

$$\begin{aligned} V_{e,r} &= V\cos(\Lambda-\beta) \\ V_{e,l} &= V\cos(\Lambda+\beta) \end{aligned} \tag{2}$$

where $V_{e,r}$ and $V_{e,l}$ is the effective speed of the right and left side, respectively.

In order to reduce the wave drag, the configuration sweep angle

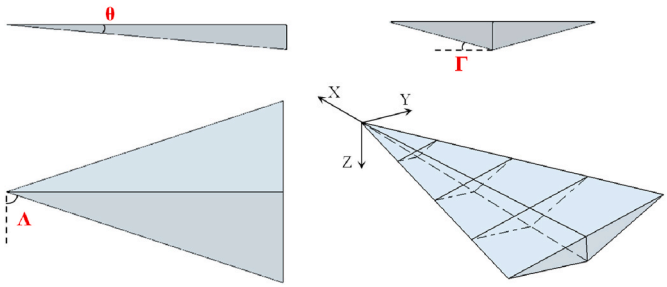

Fig. 1. Simplified geometry model.

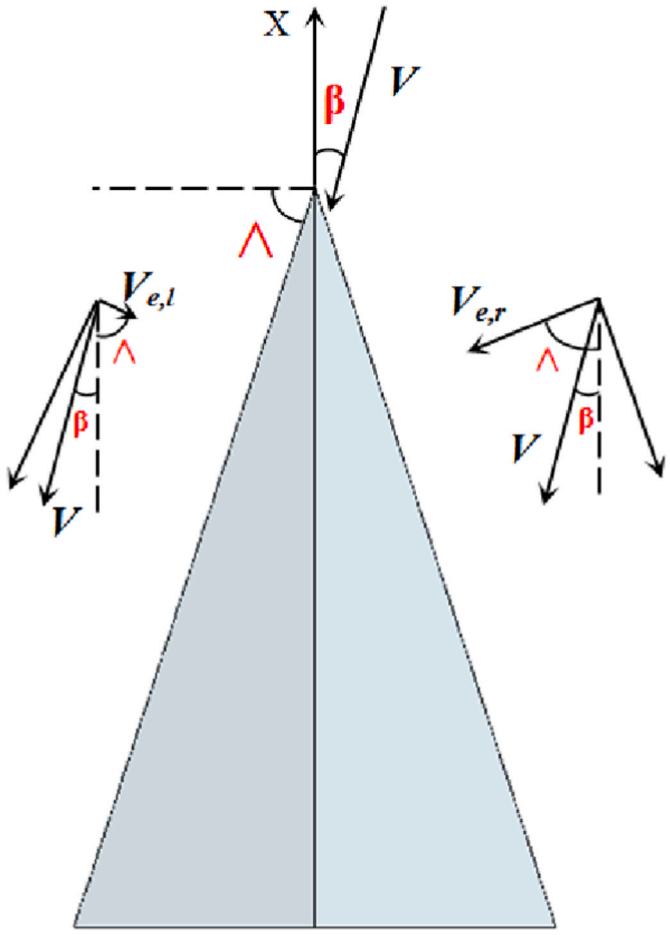

Fig. 2. Influence of sweep angle on the effective speed for each side.

usually increases as the cruise speed increases. Therefore, the sweep angle of hypersonic vehicles is generally extremely large, typically larger than 60°. Besides, the sideslip angle for hypersonic vehicles is generally minor due to the very high flight speed, typically smaller than 2°. Then a reasonable assumption can be made: $\Lambda \pm \beta \approx \Lambda$. In turn, we have: $V_{e,r} \approx V_{e,l}$, indicating that the influence of sweep angle on the lateral stability can be neglected.

In fact, pressure is basically an impact event and is little affected by the neighboring points at hypersonic conditions [15]. Then from this point of view, the influence of sweep angle may also be neglected.

Next, let's concentrate on the effect of dihedral angle. As sketched in Fig. 3, for a body with positive dihedral, due to the difference in the direction of the speed component $Vsin\beta sin\Gamma$, sideslip produces an increase in angle of attack on the right semispan and a decrease in angle of attack on the left semispan. The increment on each side can be expressed as follows

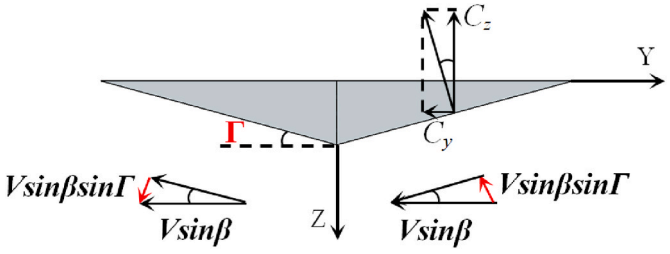

Fig. 3. Influence of dihedral angle on the effective angle of attack for each side.

$$\begin{aligned}\Delta\alpha_r &\approx \sin\Delta\alpha_r \approx \tan\Delta\alpha_r = \frac{V\sin\beta\sin\Gamma}{V\cos\beta} \approx \beta\sin\Gamma \\ \Delta\alpha_l &\approx -\beta\sin\Gamma\end{aligned} \tag{3}$$

According to the Newtonian theory, the pressure coefficient increment on the right semispan is

$$\begin{aligned}\Delta C_{p,r} &= 2\sin^2(\theta_\alpha+\Delta\alpha) - 2\sin^2\theta_\alpha \\ &= 2[\sin(\theta_\alpha+\Delta\alpha) - \sin\theta_\alpha]\cdot[\sin(\theta_\alpha+\Delta\alpha) + \sin\theta_\alpha] \\ &= 2[\sin\theta_\alpha\cos\Delta\alpha + \sin\Delta\alpha\cos\theta_\alpha - \sin\theta_\alpha]\cdot[\sin\theta_\alpha\cos\Delta\alpha + \sin\Delta\alpha\cos\theta_\alpha + \sin\theta_\alpha] \\ &\approx 2[\sin\theta_\alpha + \sin\Delta\alpha\cos\theta_\alpha - \sin\theta_\alpha]\cdot[\sin\theta_\alpha + \sin\Delta\alpha\cos\theta_\alpha + \sin\theta_\alpha] \\ &= 2\sin\Delta\alpha\cdot\cos\theta_\alpha\cdot(2\sin\theta_\alpha + \sin\Delta\alpha\cdot\cos\theta_\alpha)\end{aligned} \tag{4}$$

where $\theta_\alpha = \theta + \alpha$. And the pressure coefficient increment on the left semispan is

$$\begin{aligned}\Delta C_{p,l} &= 2\sin^2(\theta_\alpha - \Delta\alpha) - 2\sin^2\theta_\alpha \\ &= -2\sin\Delta\alpha\cdot\cos\theta_\alpha\cdot(2\sin\theta_\alpha - \sin\Delta\alpha\cdot\cos\theta_\alpha)\end{aligned} \tag{5}$$

Then the pressure coefficient increment on the lower surface can be calculated as

$$\begin{aligned}\Delta C_p &= \Delta C_{p,r} - \Delta C_{p,l} = 2\sin\Delta\alpha\cdot\cos\theta_\alpha\cdot 4\sin\theta_\alpha \\ &= 4\sin\Delta\alpha\cdot\sin 2\theta_\alpha \\ &\approx 4\beta\sin\Gamma\cdot\sin 2\theta_\alpha\end{aligned} \tag{6}$$

The pressure increment can lead to the variation of both the normal force and side force, which can be calculated as

$$\begin{aligned}\Delta C_z &= -\Delta C_p \cdot\cos\Gamma\cdot q_\infty\cdot S_{half}/(q_\infty\cdot S_{ref}) \\ &\approx -4\beta\sin\Gamma\cdot\sin 2\theta_\alpha\cdot\cos\Gamma\cdot S_{half}/S_{ref}\end{aligned} \tag{7}$$

$$\begin{aligned}\Delta C_y &= -\Delta C_p\cdot\sin\Gamma\cdot q_\infty\cdot S_{half}/(q_\infty\cdot S_{ref}) \\ &\approx -4\beta\sin\Gamma\cdot\sin 2\theta_\alpha\cdot\sin\Gamma\cdot S_{half}/S_{ref}\end{aligned} \tag{8}$$

Further assuming that the deflection angle θ, angle of attack α, and dihedral angle Γ are small, the above expressions can be simplified as

$$\Delta C_z \approx -8\beta\cdot\Gamma\cdot\theta_\alpha\cdot S_{half}/S_{ref} \tag{9}$$

$$\Delta C_y \approx -8\beta\cdot\Gamma^2\cdot\theta_\alpha\cdot S_{half}/S_{ref} \tag{10}$$

Note that both the normal force and side force can contribute to the roll moment. The corresponding roll moment coefficient produced by the normal force is

$$\begin{aligned}C_{l,1} &= \Delta C_z\cdot\bar{y}/L_{ref} \\ &\approx -8\beta\cdot\Gamma\cdot\theta_\alpha\cdot S_{half}/S_{ref}\cdot\bar{y}/L_{ref}\end{aligned} \tag{11}$$

With the reference location being chosen to be the nose, the roll moment coefficient produced by the side force is

$$\begin{aligned}C_{l,2} &= -\Delta C_y\cdot\bar{z}/L_{ref} \\ &\approx 8\beta\cdot\Gamma^2\cdot\theta_\alpha\cdot S_{half}/S_{ref}\cdot\bar{z}/L_{ref}\end{aligned} \tag{12}$$

Note that the above result is based on the constant pressure distribution assumption, which naturally holds for the simplified geometry model calculated by the Newtonian theory. In such case, the center of pressure should coincide with the centroid of the lower surface on each side, as shown in Fig. 4. The distance of centroid away from the nose can be expressed as

$$\bar{x} = \frac{2}{3}L;\ \ \bar{y} = \frac{1}{3}\frac{1}{2}b = \frac{1}{6}b;\ \ \bar{z} = \frac{1}{3}h \tag{13}$$

Assume that the reference length for roll moment is equal to $b/2$, and according to the geometric relationship, we can obtain

$$\frac{\bar{y}}{L_{ref}} = \frac{b/6}{b/2} = \frac{1}{3} \tag{14}$$

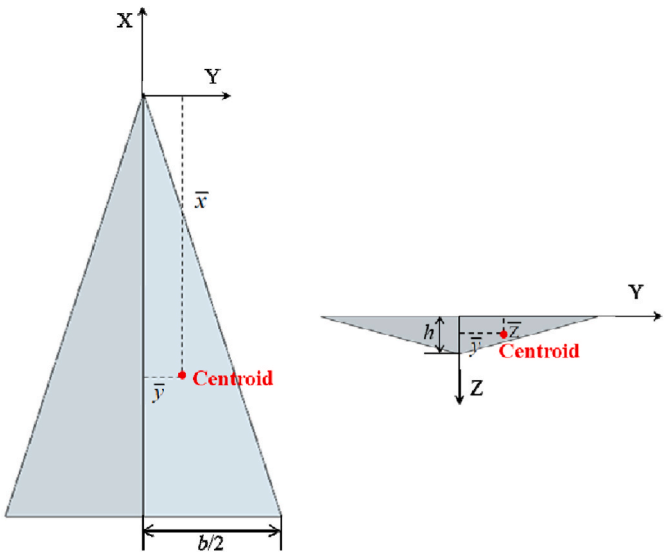

Fig. 4. Centroid of the lower surface.

$$\frac{\bar{z}}{L_{ref}} = \frac{1}{3}\cdot\frac{h}{b/2} = \frac{1}{3}\cdot\tan\Gamma \approx \frac{1}{3}\Gamma \tag{15}$$

Further assuming that the reference area is equal to S_{half}, Eqns. (11-12) can be reduced to

$$C_{l,1} \approx -\frac{8}{3}\beta\cdot\Gamma\cdot\theta_\alpha \tag{16}$$

$$C_{l,2} \approx \frac{8}{3}\beta\cdot\Gamma^3\cdot\theta_\alpha \tag{17}$$

Finally, the resultant roll moment becomes

$$\begin{aligned} C_l &= C_{l,1} + C_{l,2} \\ &\approx -\frac{8}{3}\beta\cdot\Gamma\cdot\theta_\alpha + \frac{8}{3}\beta\cdot\Gamma^3\cdot\theta_\alpha \\ &\approx -\frac{8}{3}\beta\cdot\Gamma\cdot\theta_\alpha\left(1-\Gamma^2\right) \end{aligned} \tag{18}$$

For small dihedral angle, we have $\Gamma^2 \ll 1$. Then Eqn. (18) can be finally simplified as

$$C_l \approx -\frac{8}{3}\beta\cdot\Gamma\cdot\theta_\alpha \tag{19}$$

The above result implies that for the roll moment, the influence of side force can almost be neglected. In fact, when the reference location moves downward along the Z-axis, the contribution of side force to the roll moment would become smaller in that the moment of the upper and lower part can be counteracted mutually.

Hence, based on the expression of $C_{l,1}$, the roll stability derivative $C_{l\beta}$ becomes

$$\begin{aligned} C_{l\beta} &\approx -8\Gamma\cdot\theta_\alpha\cdot\frac{\bar{y}}{L_{ref}}\cdot\frac{S_{half}}{S_{ref}} \\ &\approx -\frac{8}{3}\Gamma\cdot\theta_\alpha \end{aligned} \tag{20}$$

The above equation can clearly reveal the dominant influence of geometric parameters and angle of attack on the roll stability derivative. It can be found that the lateral static stability increases linearly as the deflection angle, dihedral angle, or angle of attack increases at hypersonic conditions.

2.3. Directional static derivative $C_{n\beta}$

According to Eqn. (10), the side force static derivative can be expressed as

$$\begin{aligned} C_{y\beta} &\approx -8\Gamma^2\cdot\theta_\alpha\cdot S_{half}/S_{ref} \\ &\approx -8\Gamma^2\cdot\theta_\alpha \end{aligned} \tag{21}$$

The yaw moment is mainly produced by the side force. Again we assume that the pressure distribution is constant and the reference location is chosen to be the nose of the model, the directional stability derivative $C_{n\beta}$ can be expressed as

$$\begin{aligned} C_{n\beta} &= -C_{y\beta}\cdot\bar{x}/L_{ref} \\ &\approx -8\Gamma^2\cdot\theta_\alpha\cdot\frac{S_{half}}{S_{ref}}\cdot\frac{\bar{x}}{L_{ref}} \end{aligned} \tag{22}$$

Assuming that the reference length for the yaw moment is equal to L, the equation can be further reduced to

$$C_{n\beta} \approx -\frac{16}{3}\Gamma^2\cdot\theta_\alpha \tag{23}$$

The above equation can clearly reveal the dominant influence of geometric parameters and angle of attack on the yaw stability derivative. By comparing Eqn. (20) and Eqn. (23), we can find that the formulas of the two static derivatives are quite close. The main difference lies in that $C_{n\beta}$ is proportional to Γ^2 while $C_{l\beta}$ is proportional to Γ, indicating that the increase of dihedral angle has a more prominent influence on the improvement of directional static stability.

3. Computational-Fluid-Dynamics solver

The CFD results will be used to validate the accuracy of the simplified models and analyze the influence of viscous effects. Thus, the numerical methods are described in this section, along with the validation of chemical nonequilibrium models and the grid independence.

3.1. Numerical methods

The steady-state inviscid, laminar, and turbulent flow numerical simulations are performed in this paper. A cell-centered finite volume method is employed to solve the three-dimensional compressible Euler, Navier-Stokes, or Reynolds-Averaged Navier-Stokes equations. The AUSM + spatial discretization scheme is adopted, with an implicit lower-upper symmetric Gauss-Seidel scheme for the temporal integration to accelerate convergence. For the laminar flow simulations, both the calorically perfect gas model and non-equilibrium reacting gas model are adopted and compared to examine the influence of the real gas effects. For the turbulent flow simulations, the 3-equation *k-ε-Rt* model is adopted [16]. For the chemical nonequilibrium simulations, a modified Fick's model is applied to calculate the species mass diffusion fluxes, ensuring that the sum of individual species' diffusion fluxes is zero [17]. The transport properties of mixture species are calculated according to Gupta's mixing rule [18], and the viscosity and thermal conductivity of species are calculated using collision cross-section data compiled by Wright [19]. More details about the CFD solver and its validation for hypersonic laminar and turbulent flows with the calorically perfect gas model can be found in Refs. [9,20,21].

For the nonequilibrium reacting gas model, the hypersonic cylinder flow experiment by Hannemann et al. [22] in DLR is selected as the validation case. The radius of the cylinder is 0.045 m. The freestream condition in the experiment, along with the gas species, is listed in Table 1. The freestream Reynolds number and Knudsen number based

Table 1
Freestream condition for the DLR cylinder experiment [22].

P_∞(Pa)	T_∞(K)	u_∞(m/s)	ρ_∞(kg/m^3)	M_∞
687	694	4776	0.00326	8.78
ξ_{N_2}	ξ_{O_2}	ξ_{NO}	ξ_N	ξ_O
0.73555	0.134	0.0509	1.0e-9	0.07955

on the radius is 2.11×10^{-4} and 5.44×10^{-4}, respectively (the viscosity coefficient is 3.31×10^{-5}kg/(m·s) and the mean free path is 2.45×10^{-4} m). Therefore, the fully laminar model is adopted without considering the slip effects. In addition, the chemical reaction model in numerical simulations is the 5-species gas and 6-reaction model developed by Gupta et al. [18], as given in Table 2. The above calculate methods are the same as those used in Ref. [22]. The three-dimensional computation is performed and the grid is shown in Fig. 5.

Note that the streaming cylinder is very often unstable causing the formation and separation of vortexes periodically from the opposite edges and the presence of chemical reactions contributes to the arising instability [23,24]. Therefore, the unsteady simulation is performed based on the steady result with the time step being 1×10^{-6}s. The pressure and Mach contours at the symmetry plane at different time steps around the cylinder are given in Fig. 6. It can be found that at such condition, the vortexes around the opposite edge have no influence on the flow around the windward side. Furthermore, the pressure distribution along the wall and the density distribution along the stagnation streamline at the symmetry plane from the current solver are compared with those from the experiment and the DLR CEVCATS-N code, which are plotted in Fig. 7. It is shown that the pressure distribution from the chemical nonequilibrium model agrees very well with the experiment data, with the deviation of the stagnation pressure being only 2.22%. And the deviation of the shock stand-off distance from the experiment ($0.265R$) is only 0.75% for the current result ($0.263R$). The distribution is rather identical for the two numerical results. Note that the difference of the density distribution near the shock wave between CFD and experiment is mainly due to the expansion of the freestream caused by the conical nozzle [22]. The above results demonstrate that the current solver is reliable for hypersonic flow simulations with chemical reactions.

3.2. Grid independence validation

The geometry model defined by the parameter combination $\theta = 5^\circ$ and $\Gamma = 15^\circ$ is taken here to conduct the grid independence validation. The number of the coarse and refined grid is about 6,000,000 (Fig. 8) and 12, 000, 000 cells, respectively. The latter one is refined on the surface for about two times based on the coarse grid. The first grid spacing normal to the wall is 1×10^{-5} m, being small enough to satisfy $y+\leq 1$. And the near field domain around the lower surface is specially refined to better capture the shock wave. The calculate condition is: $M_\infty = 20$, $H = 60$ km, $\alpha = 0^\circ$, and $\beta = 2^\circ$. The corresponding freestream Reynolds number is 1.2×10^5, and thus the fully laminar model with an isothermal wall condition $T_w = 1000$ K is adopted. For the chemical nonequilibrium simulations, the 5-species air and 6-reaction model (Table 2) are employed, along with the fully catalytic wall.

The comparison of aerodynamic forces is given in Table 3, including the inviscid and laminar simulations with different gas models. We can find that the results from the two grids are extremely coincident, with the largest relative difference being only 0.94% (Laminar-RG, C_l). Therefore, the coarse grid is used herein to save the computational costs.

In addition, the temperature contours at the symmetry plane and temperature distribution at different cross sections for different gas models are shown in Figs. 9 and 10. We can find that the temperature is reduced by the chemical reactions, but the maximum temperature in the flowfield is no more than 5000K for the two models. Therefore, the current reaction models without ionization are sufficient to capture the chemical nonequilibrium effects.

Table 2
Chemical reactions and reaction rate coefficients of the Gupta model [18].

No.	Reaction	A_{fr}	B_{fr}	C_{fr}	A_{br}	B_{br}	C_{br}
1	$O_2 + I_1 \Leftrightarrow 2O + I_1$	3.61e18	59400	−1	3.01e15	0	−0.5
2	$N_2 + I_2 \Leftrightarrow 2N + I_2$	1.92e17	113100	−0.5	1.09e16	0	−0.5
3	$N_2 + N \Leftrightarrow 2N + N$	4.15e22	113100	−1.5	2.32e21	0	−1.5
4	$NO + I_3 \Leftrightarrow O + N + I_3$	3.97e20	75600	−1.5	1.01e20	0	−1.5
5	$NO + O \Leftrightarrow O_2 + N$	3.18e9	19700	1	9.63e11	3600	0.5
6	$N_2 + O \Leftrightarrow NO + N$	6.75e13	37500	−1	1.50e13	0	0

I_1: O, N, O_2, N_2, NO; I_2: O, O_2, N_2, NO; I_3: O, N, O_2, N_2, NO.

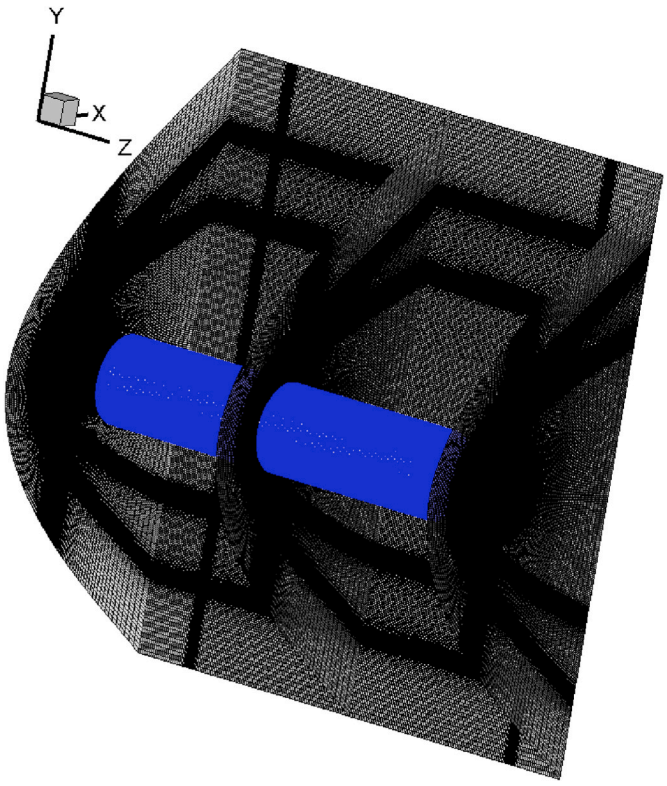

Fig. 5. Three-dimensional grid around the cylinder.

3.3. Accumulation of error

Because the governing equations are discretized and solved on finite grid size, a definite error occurs in integration at each step and the accumulation of error is proportional to the number of integration steps [25]. The integration steps should not exceed the maximal allowable steps that accumulated error exceeds the acceptable value. The maximal allowable number of integration steps is determined by [25].

$$n_{\max} = \left(S^{\max}/S_{err}\right)^2 \tag{24}$$

where $S^{\max}$ is total error and it is presumed to be between 1% and 5%. $S_{err} \approx \sum_{i=1}^{3} S_i$ and S_i is the relative error of integration in one dimensional case and defined as

$$S_i \approx \left(\Delta L/L_i\right)^{k+1} \tag{25}$$

where $\triangle L$ is the mean cell size and L_i is the domain size in the "i" direction, k is the order of accuracy of numerical scheme. The ratio of maximal allowable and actual number of integration steps is defined as follow, which tends to unit when the accumulate error tends to the maximal allowable value.

$$R_s = \frac{n_{\max}}{n} \tag{26}$$

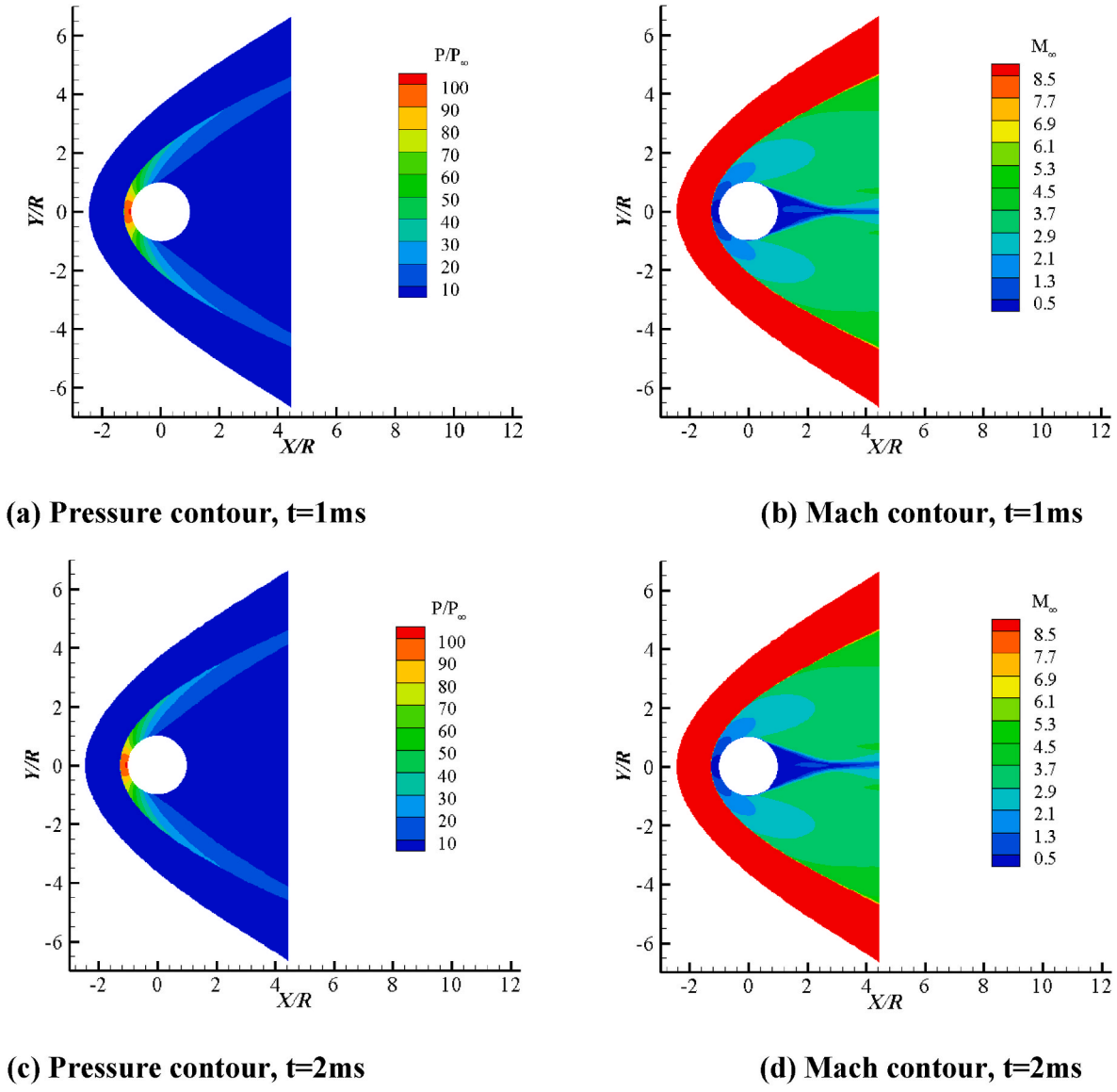

Fig. 6. Flow contour at the symmetry plane at different time steps.

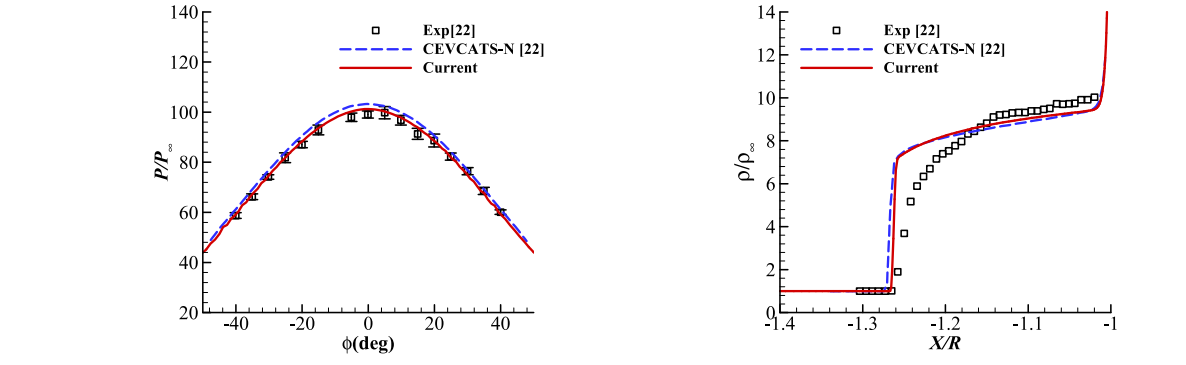

Fig. 7. Comparison of flow characteristics at the symmetry plane.

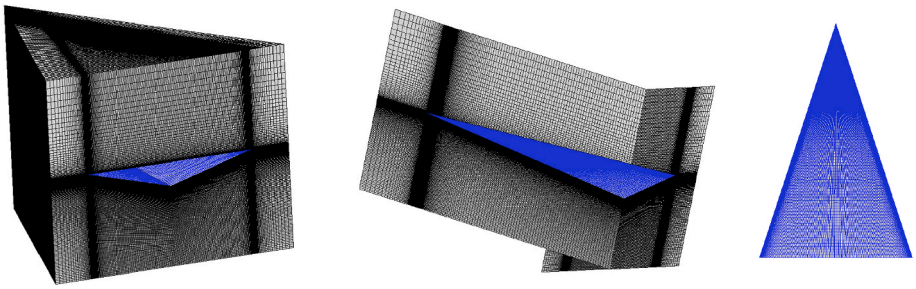

Fig. 8. Coarse grid used in numerical simulations (about 6,000,000 cells).

Table 3
Comparison of aerodynamic forces between different grids.

	$C_y \times 10^{-3}$		$C_l \times 10^{-3}$		$C_n \times 10^{-3}$	
	Coarse	Refined	Coarse	Refined	Coarse	Refined
Euler	−1.879	−1.877	−2.235	−2.235	1.324	1.323
Laminar-PG	−2.792	−2.811	−2.833	−2.860	2.150	2.167
Laminar-RG	−2.697	−2.704	−2.669	−2.682	2.083	2.090

For the coarse grid, the number of grid points along the streamwise, spanwise, and normal direction is 191, 188, and 192, respectively. And the aerodynamic forces for the coarse grid can be converged by nearly 20,000 steps. The corresponding accumulate error is listed in Table 4. It's clear that the present simulations have high reliability in terms of accumulate error.

4. Model validation

Three different configurations are chosen to validate the accuracy of the simplified analytical models. As sketched in Fig. 11, the parameter combinations are (θ, Γ) are (5°, 15°), (5°, 20°), and (10°, 20°), respectively. Note that all the configurations are 1 m long without special instructions.

The accuracy of Newtonian theory improves as the Mach number increases. Therefore, the influence of Mach number on the static derivatives is first studied based on the inviscid CFD solutions of the configuration θ = 5° and Γ = 15°, shown in Fig. 12. Note that the static derivatives from CFD are calculated by the linear interpolation of the forces or moments at $\beta = 2°$. It can be found that both the lateral and directional static stability decreases as the Mach number increases. The difference of results between Mach 5 and Mach 10 is significant, but all the derivatives are almost kept unchanged above Mach 15.

Based on the above influence of Mach number, the comparison of derivatives for the three typical configurations at $M_\infty = 20$ is given in Fig. 13. Note that the results of the model correspond to those calculated

Table 4
Accumulate error.

S_1	S_2	S_3	S_{err}	S^{max}	n	n_{max}	R_s
1.44×10^{-7}	1.51×10^{-7}	1.41×10^{-7}	4.36×10^{-7}	0.05	20,000	1.32×10^{10}	6.6×10^{5}

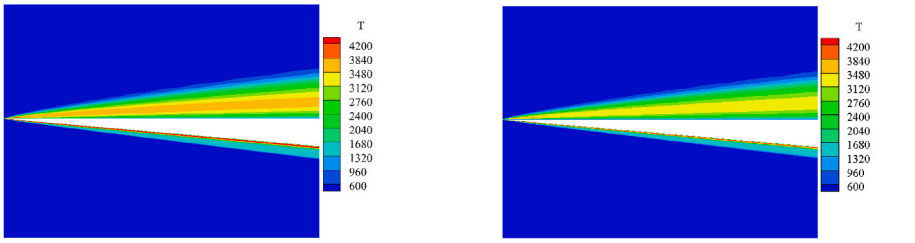

Fig. 9. Temperature contours at the symmetry plane for different gas models, α = 8°.

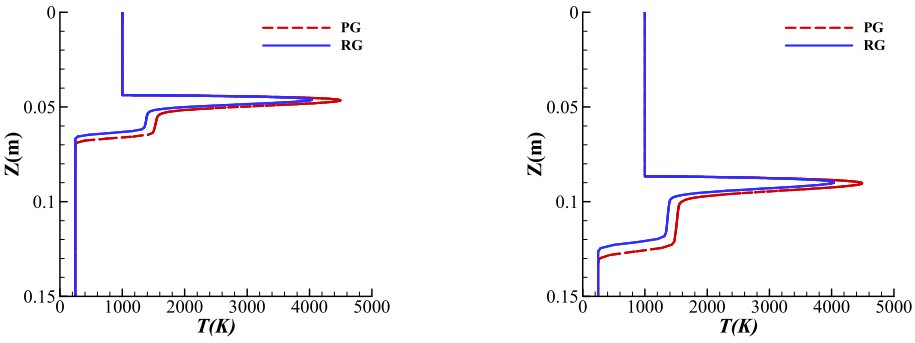

Fig. 10. Comparison of temperature distribution around the lower surface at different cross sections, α = 8°.

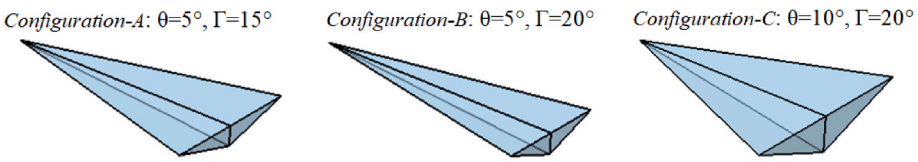

Fig. 11. Configurations with different parameter combinations.

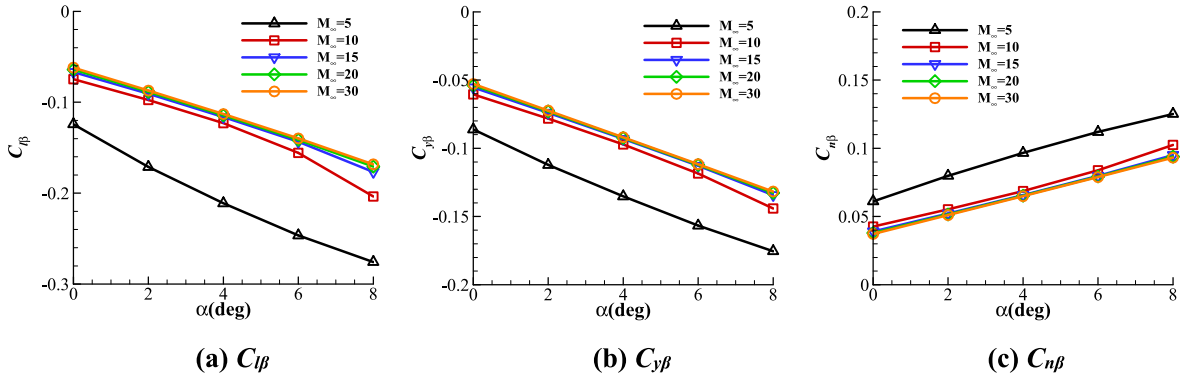

Fig. 12. Comparison of derivatives at different Mach numbers from inviscid CFD solutions.

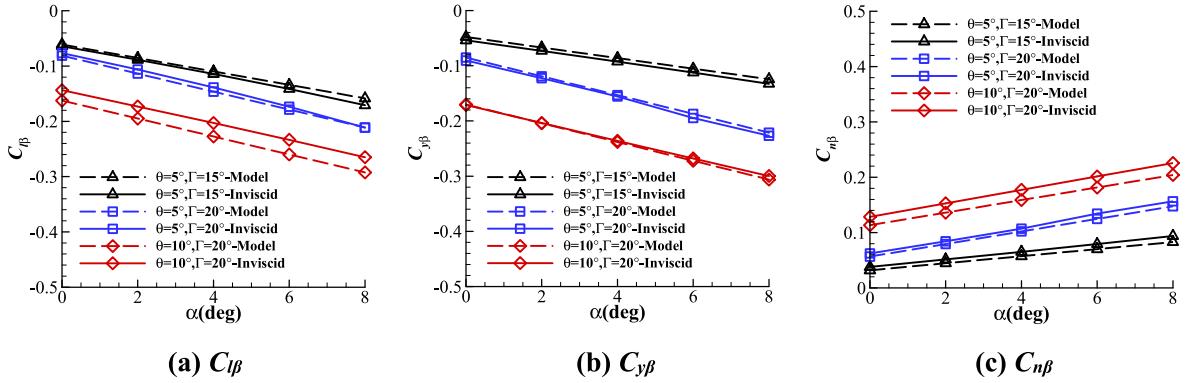

Fig. 13. Comparison of derivatives for different configurations, $M_\infty = 20$.

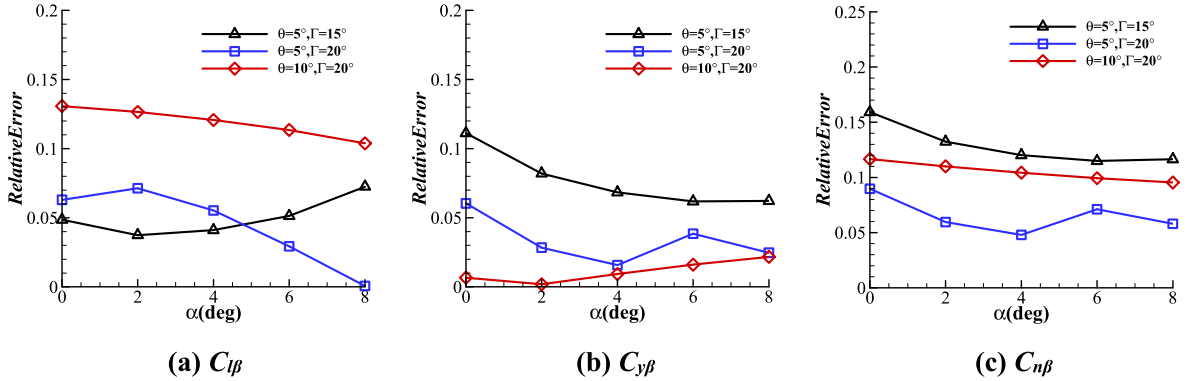

Fig. 14. Relative errors of analytical models for different configurations, $M_\infty = 20$.

by Eqns. (20), (21) and (23). It can be found that good agreement between the analytical models and CFD is obtained. And as shown in Fig. 14, most relative errors are no more than 15%. Especially, the slope of curve is well predicted for different configurations. Such results demonstrate that the derivation is reasonable, and the analytical models can be considered quite acceptable to capture and analyze the dominant geometric influence on the lateral-directional static stability.

According to the derivation process, the errors of analytical models mainly result from the application of Newtonian theory, the sweep independence approximation, and the constant pressure distribution assumption on each side. As for the last factor, the inviscid pressure contour is illustrated in Fig. 15. It shows that the pressure near the

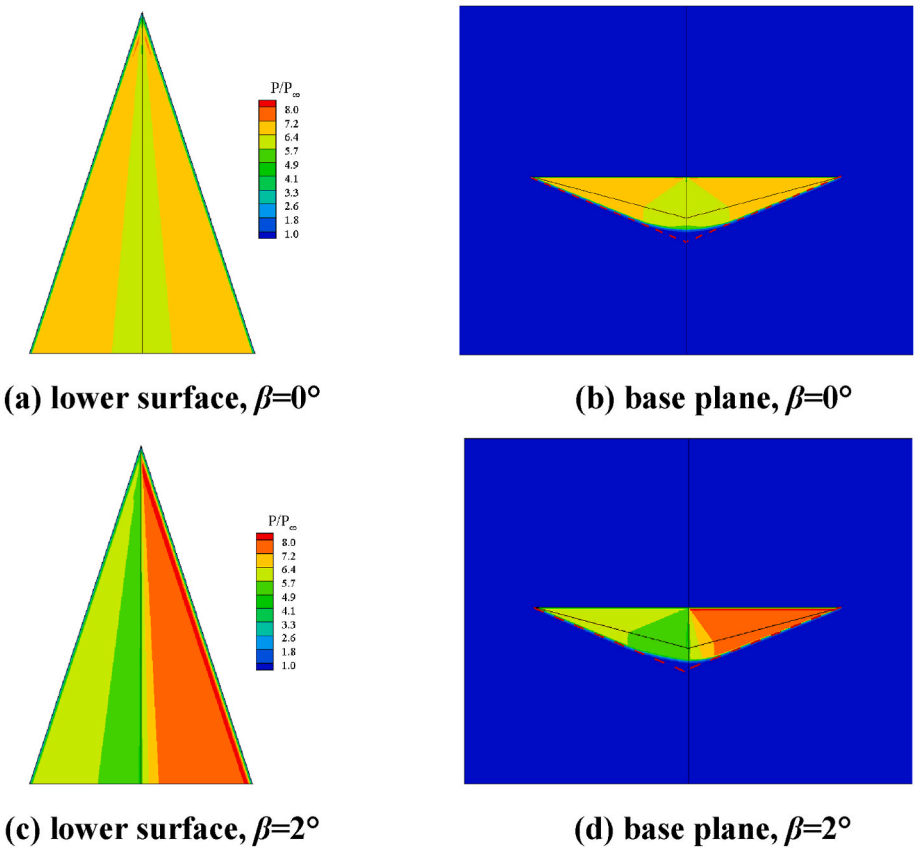

Fig. 15. Inviscid pressure contour at the condition: $M_\infty = 20$, $\alpha = 0°$ ($\theta = 5°$, $\Gamma = 15°$).

symmetry plane is lower (the region of pressure dip, called later) than that of the other region on each side, which is mainly attributed to the three-dimensional flow effects.

5. Influence of viscous effects

The influence of viscous effects on the aerodynamic performance is of vital importance especially at hypersonic conditions. For example, the comparison of the inviscid and laminar lift-to-drag ratio (L/D) is given in Fig. 16(a) at the condition of $M_\infty = 20$, $H = 60$ km. It is clear that the L/D is greatly reduced when the viscous effects are taken into account, which is mainly attributed to the drag increase as shown in Fig. 16(b).

In order to analyze the influence of viscous effects on stability derivatives, which cannot be directly captured by the above simplified models, the inviscid and viscous CFD results for different configurations are compared in Figs. 17–19 at the condition of $M_\infty = 20$, $H = 60$ km. Note that *Laminar-inv* and *Laminar-total* denotes the inviscid components and the total components (including the force integral of shear stress) from the laminar perfect gas model, respectively. It can be observed that both the lateral and directional stability are improved evidently by the viscous effects.

It's well known that for hypersonic flight, the high altitude and large Mach number may lead to a thick hypersonic boundary layer, which displaces the outer inviscid flow and changes its nature. In turn, the substantial changes on the outer inviscid flow may feedback to the boundary layer, affecting its growth and properties. Such mutual interaction process is called the strong viscous interaction [26]. Therefore, the influence of viscous effects at hypersonic conditions can be decomposed into two aspects, including the induced pressure caused by the strong viscous interaction and the shear stress.

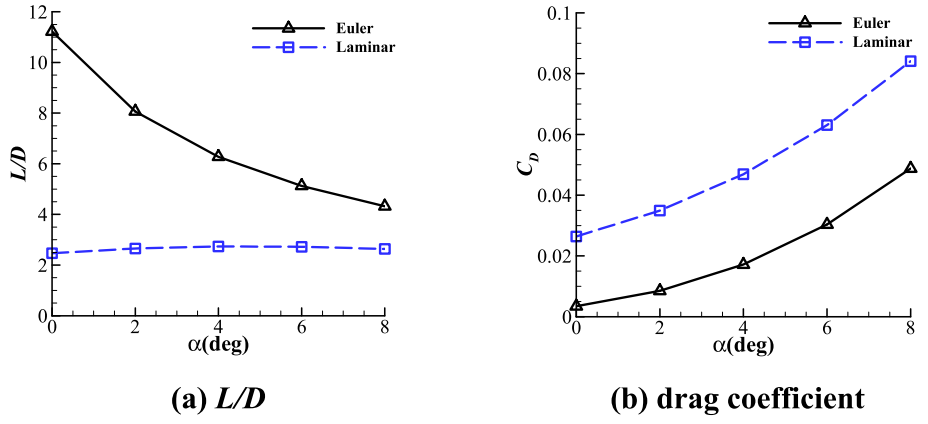

Fig. 16. Comparison of L/D and drag coefficient at different calculate conditions ($\theta = 5°$, $\Gamma = 15°$).

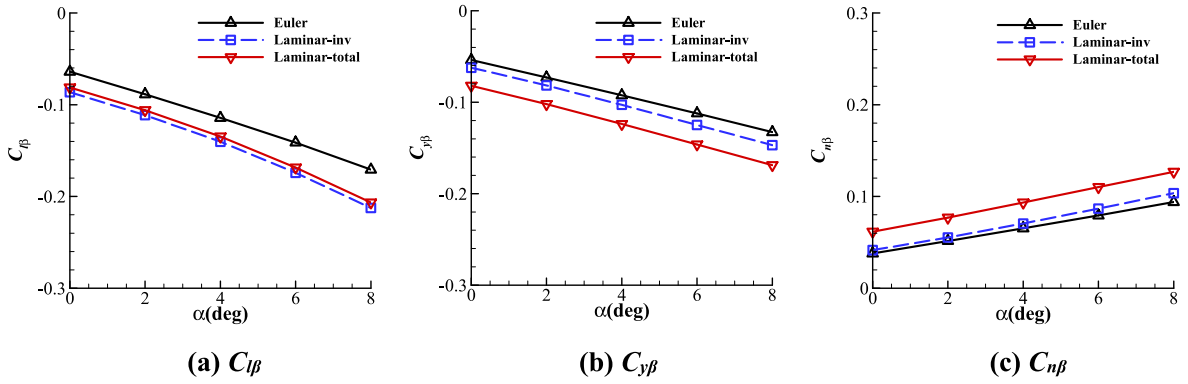

Fig. 17. Comparison of derivatives at different calculate conditions (θ = 5°, Γ = 15°).

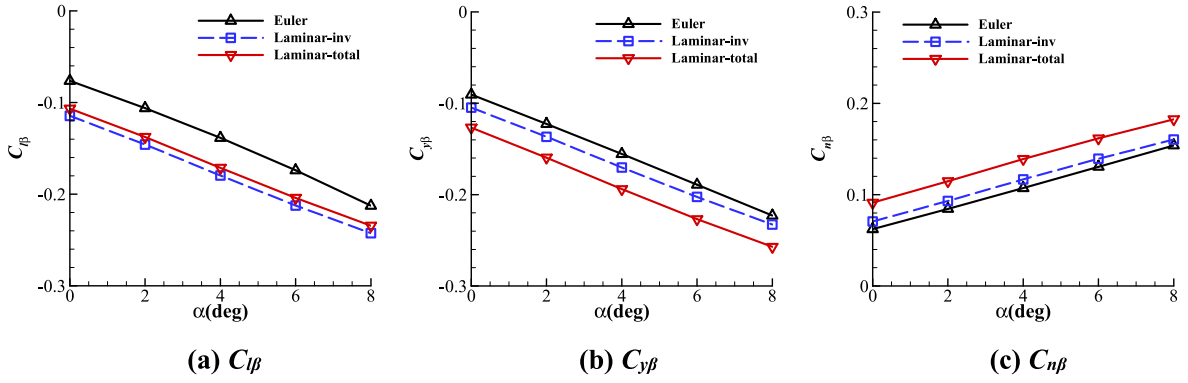

Fig. 18. Comparison of derivatives at different calculate conditions (θ = 5°, Γ = 20°).

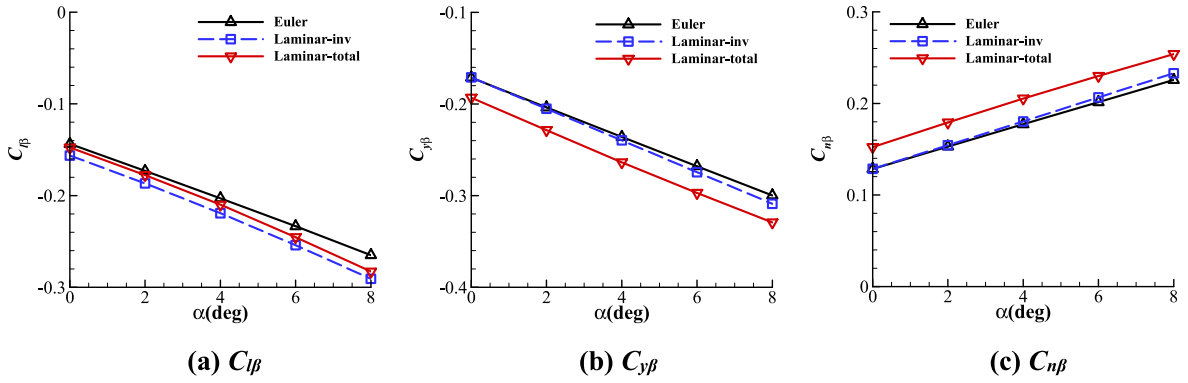

Fig. 19. Comparison of derivatives at different calculate conditions (θ = 10°, Γ = 20°).

First, by comparing the derivatives from *Euler* and *Laminar-inv*, both the lateral and directional stability are improved, while the improvement of the lateral stability is evidently larger than that of the directional stability. In order to explain this phenomenon, the comparison of pressure distribution at the base plane is given in Figs. 20 and 21. It can be found that at the same flight condition, the laminar pressure is apparently larger than the inviscid pressure, which results from the hypersonic strong viscous interaction effects. In fact, in terms of the pressure variation, the influence of viscous interaction is somewhat equivalent to the increase of angle of attack, especially near the leading edge where the viscous interaction is stronger. Then according to Eqn. (6), the pressure increment caused by sideslip should increase when the viscous effects are considered. However, only the distribution near the leading edge (region I and IV) is consistent with the above analysis, while the distribution near the symmetry plane (region II and III) is just opposite.

Such results can be mainly attributed to the three-dimensional flow effects. From the inviscid pressure distribution shown in Fig. 22, an evident boundary exists between the pressure dip near the symmetry plane and the region where the pressure is almost uniform. The boundary moves left for positive sideslip, leading to the local increase of pressure increment. And as the angle of attack increases, the pressure dip turns larger, making the region of the local increase move outward. The result is that the pressure increment caused by the strong viscous interaction is partly counteracted by the three-dimensional flow effects. However, for the roll moment, the arm of force near the symmetry plane (region II and III) is shorter than that near the leading edge (region I and IV), weakening the influence of three-dimensional flow effects on the lateral stability. Therefore, for the inviscid components, the improvement of the lateral stability is evidently larger than that of the

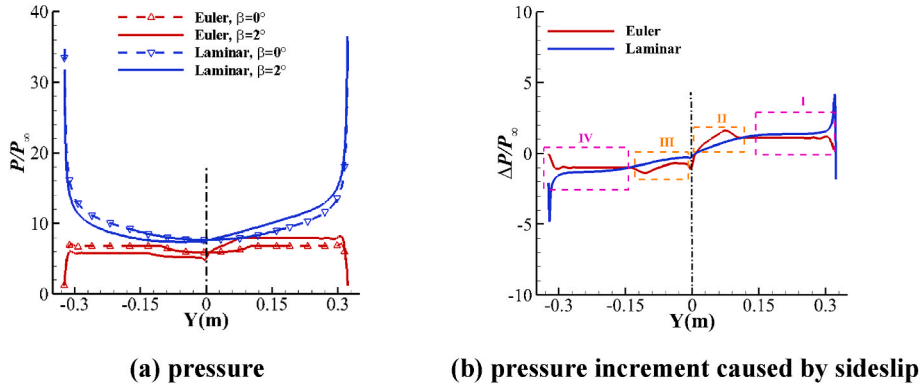

Fig. 20. Comparison of dimensionless pressure distribution at the base plane, $\alpha = 0°$ ($\theta = 5°$, $\Gamma = 15°$).

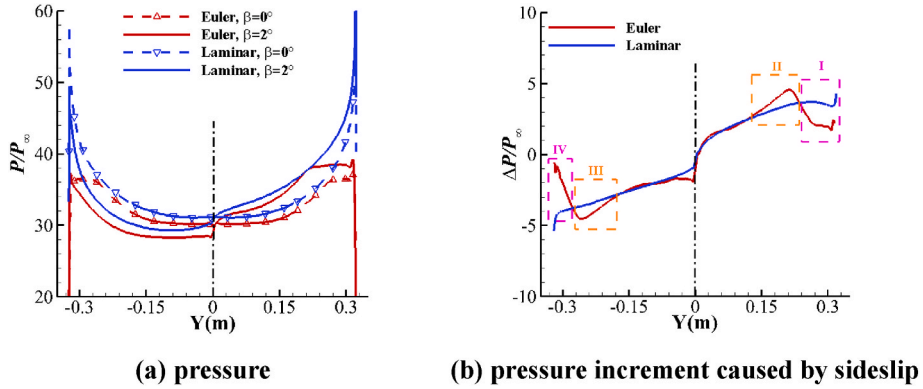

Fig. 21. Comparison of dimensionless pressure distribution at the base plane, $\alpha = 8°$ ($\theta = 5°$, $\Gamma = 15°$).

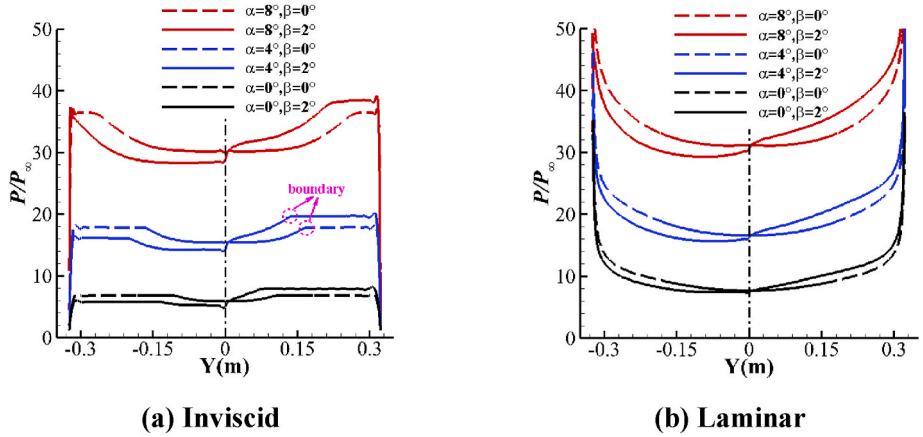

Fig. 22. Comparison of pressure distribution at the base plane ($\theta = 5°$, $\Gamma = 15°$).

directional stability.

The influence of the shear stress can be analyzed by comparing the derivatives from *Laminar-inv* and *Laminar-total*. As shown in Fig. 22(b), the positive sideslip changes the distribution of transverse pressure gradient, making the shear stress component τ_y increase at the right side and decrease at the left side, which is shown in Fig. 23. However, the variation of the normal component τ_z is very minor. Therefore, the shear stress mainly affects the side force and leads to an evident improvement of the directional stability.

Furthermore, the comparison of derivatives between the laminar perfect gas model and chemical nonequilibrium model is plotted in Fig. 24. It can be found that the chemical nonequilibrium effects have a more prominent influence on the lateral stability, with the maximum relative variation being 7.95% ($\alpha = 8°$). The reason can be explained according to Figs. 25 and 26, where the comparison of the pressure and shear stress distribution is plotted, respectively. At the same flight condition, the chemical reactions can decrease the wall pressure. Besides, the pressure increment caused by sideslip is also reduced near the leading edge, implying that the influence of strong viscous interaction can be weakened by the chemical nonequilibrium effects. However, the shear stress component τ_y and $\triangle\tau_y$ caused by sideslip is little affected. Therefore, the lateral stability is slightly reduced and the directional stability is almost unchanged by the chemical reactions.

Finally, the fully laminar and turbulent results with perfect gas

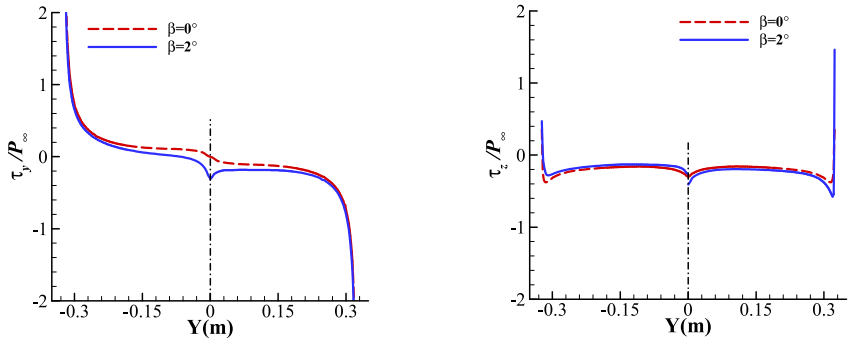

Fig. 23. Comparison of shear stress distribution at the base plane, α = 8° (θ = 5°, Γ = 15°).

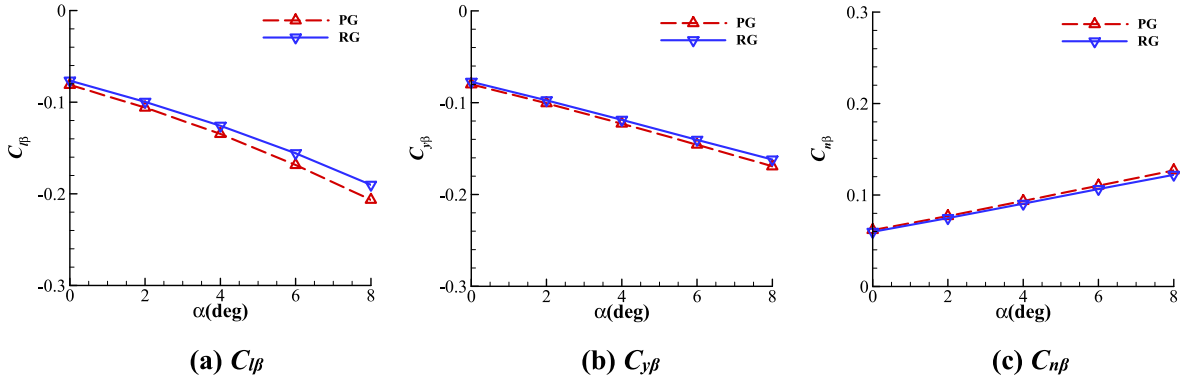

Fig. 24. Comparison of derivatives with different gas models (θ = 5°, Γ = 15°).

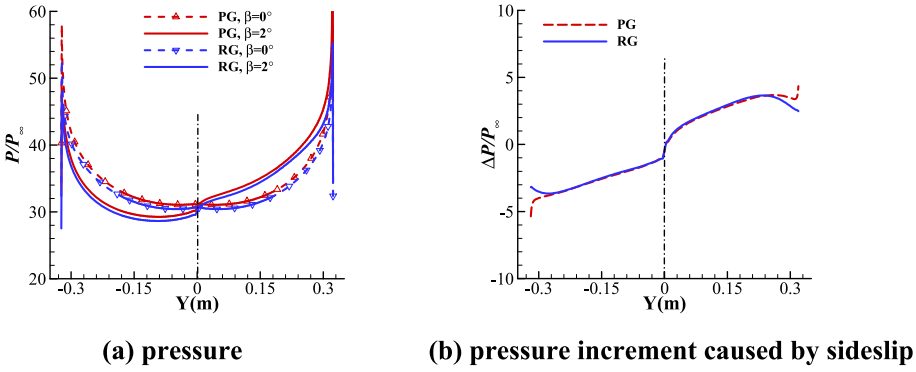

Fig. 25. Comparison of dimensionless pressure distribution at the base plane, α = 8°.

model are compared in Fig. 27 at the condition of $M_\infty = 20$, $H = 40$ km for the configuration with $L = 10$ *m*. In such condition, the Reynolds number is 1.58×10^7 and the turbulent effects should be considered. Compared with the laminar results, the turbulent flow mainly improves the directional stability, with the maximum relative variation being 9.51% (α = 0°). This phenomenon can be explained according to Figs. 28 and 29. It is observed that at the same flight condition, the turbulent flow makes the wall pressure higher, but the pressure increment caused by sideslip is only slightly altered. As a result, the lateral stability is only improved by 3.32% at α = 8°. As expected, the main difference lies in the shear stress τ_y and the increment caused by sideslip is higher for the turbulent flow, leading to the more evident improvement of the directional stability.

6. Conclusions

Analytical models of lateral-directional static derivatives are proposed based on the simplified geometry model, which can directly reveal the relationship between the geometric features and the stability. It's found that the lateral and directional stability both increase as the deflection angle, dihedral angle, or angle of attack increases, whereas the influence of sweep angle can be neglected. The difference lies in that the directional stability is proportional to the square of dihedral angle while the lateral stability is proportional to dihedral angle, indicating that the dihedral angle has a more prominent influence on the directional static stability. In addition, the influence of side force on the lateral stability can be neglected. The reasonable accuracy of the models is validated in comparison with the inviscid numerical solutions. Furthermore, based on the numerical results, it's found that both the

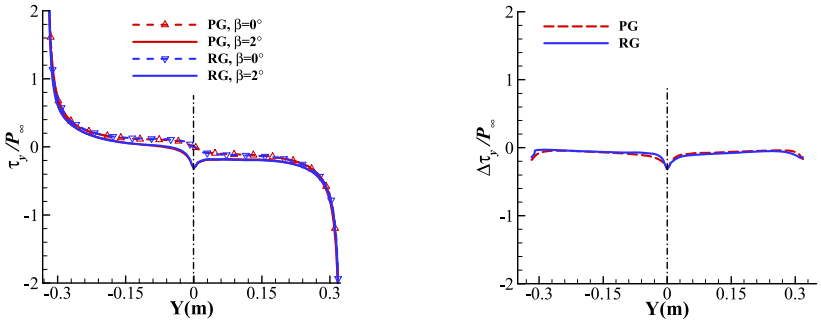

(a) shear stress (b) shear stress increment caused by sideslip

Fig. 26. Comparison of dimensionless shear stress distribution at the base plane, α = 8°.

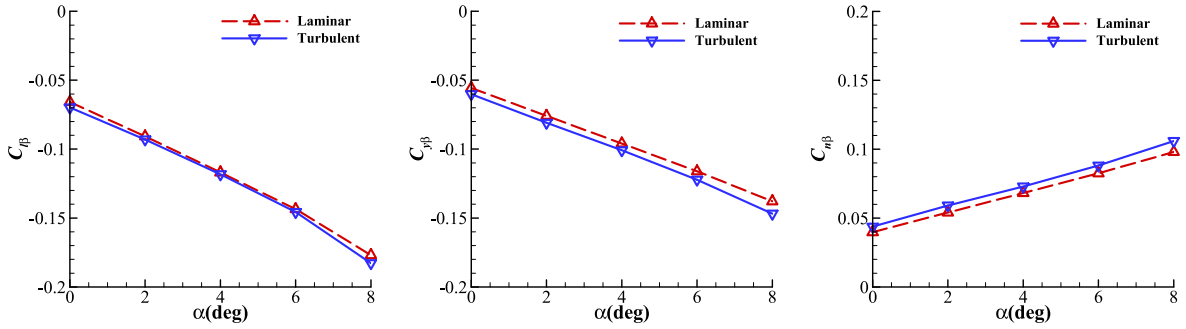

(a) $C_{l\beta}$ (b) $C_{y\beta}$ (c) $C_{n\beta}$

Fig. 27. Comparison of derivatives with different viscous models (θ = 5°, Γ = 15°).

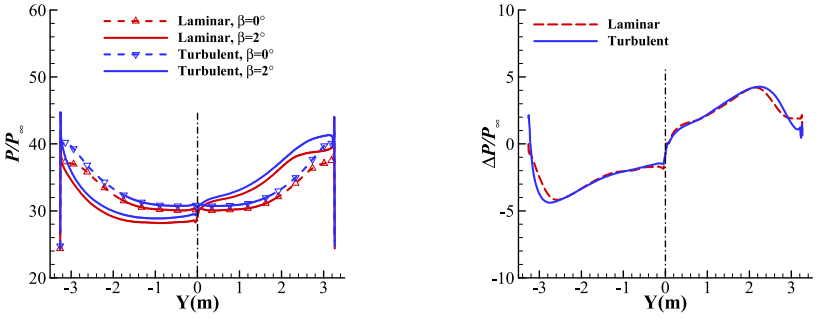

(a) pressure (b) pressure increment caused by sideslip

Fig. 28. Comparison of dimensionless pressure distribution at the base plane, α = 8°.

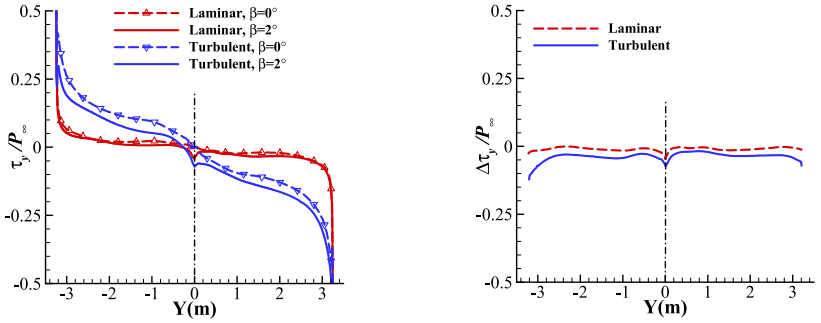

(a) shear stress (b) shear stress increment caused by sideslip

Fig. 29. Comparison of dimensionless shear stress distribution at the base plane, α = 8°.

lateral and directional stability are improved by the viscous effects. Specifically, the variation of lateral stability is mainly affected by the strong viscous interaction, and the variation of directional stability is affected by both the strong viscous interaction and the shear stress. In addition, the lateral stability is slightly reduced and the directional stability is almost unchanged by the chemical nonequilibrium effects.

In summary, according to the analytical models proposed in this paper, there are fundamental differences in the hypersonic lateral-directional static stability compared with the conventional theory of flight dynamics. And the deflection angle and dihedral angle should be especially concerned to achieve excellent lateral-directional stability design and optimization for hypersonic vehicles. In the future, the simplified models can be combined with data-driven methods, such as the machine learning symbolic regression, to construct the stability models for more complex hypersonic configurations, such as the waverider.

Declaration of competing interest

The authors declare that they have no known competing financial interests or personal relationships that could have appeared to influence the work reported in this paper.

Acknowledgments

This work was supported by the National Natural Science Foundation of China (11902324) and the Strategic Priority Research Program (A) of Chinese Academy of Science (XDA17030000). The authors would also be very grateful to the reviewers for their thoughtful suggestions that have helped to improve this paper substantially.

References

[1] D.T. McRuer, I.L. Ashkenas, D. Graham, Aircraft Dynamics and Automatic Control, Princeton Univ. Press, Princeton, NJ, 1973, p. 354.
[2] D.B. Johnson, R. Thomas, D. Manor, Stability and control analysis of a waverider TSTO second stage, in: AIAA/NAL-NASDA-ISAS 10th International Space Planes and Hypersonic Systems and Technologies Conference, AIAA, April 2001. Paper 2001-1834.
[3] C.E. Cockrell, L.D. Huebner, D.B. Finley, Aerodynamic Characteristics of Two Waverider-Derived Hypersonic Cruise Configurations, NASA, July 1996. Technical Paper 3559.
[4] M. Rasmussen, Effects of Anhedral and Finlets on Lateral Stability of Hypersonic Waveriders," *35th AIAA Aerospace Sciences Meeting & Exhibit*, AIAA, Jan. 1997. Paper 1997-0191.
[5] G. Pezella, Aerodynamic and aerothermodynamic trade-off analysis of A small hypersonic flying test bed, Acta Astronaut. 69 (April 2011) 209–222, https://doi.org/10.1016/j.actaastro.2011.03.004.
[6] T. Bykerk, D. Verstraete, J. Steelant, Low speed lateral-directional aerodynamic and static stability analysis of A hypersonic waverider, Aero. Sci. Technol. 98 (Jan. 2020) 1–15, https://doi.org/10.1016/j.ast.2020.105709.
[7] Y.M. Shang, R.H. Hua, X.X. Yuan, Etc., "Research on rolling stability of the flexible waverider based on computational fluid dynamics/computational structural dynamics/rigid body dynamics coupling methodology, Proc. IME G J. Aero. Eng. (Dec. 2021) 1–13, https://doi.org/10.1177/09544100211059630. Vol. 0, No. 0.
[8] A. Aprovitola, L. Iuspa, G. Pezzella, A. Viviani, Phase-A design of A reusable Re-entry vehicle, Acta Astronaut. 187 (June 2021) 141–155, https://doi.org/10.1016/j.actaastro.2021.06.034.
[9] W. Liu, C.A. Zhang, X.P. Wang, J.J. Li, Etc., "parametric study on lateral-directional stability of hypersonic waverider, AIAA J. 59 (No. 8) (Aug. 2021) 3025–3042, https://doi.org/10.2514/1.J059904.
[10] W.F. Phillips, Analytical solution for wing dihedral effect, J. Aircraft 39 (3) (Feb. 2002) 514–516, https://doi.org/10.2514/2.2960.
[11] T. Linehan, K. Mohseni, Theoretical prediction of roll moment due to sideslip for thin low-aspect-ratio wings, AIAA J. 57 (No. 4) (April 2019) 1452–1467, https://doi.org/10.2514/1.J057160.
[12] W.H. Mason, Configuration Aerodynamics, Virginia Tech, Blacksburg, 2006. Chaps. 4 and 11.
[13] Z.A. Jia, C.A. Zhang, K.M. Wang, F.M. Wang, Longitudinal static stability analysis of hypersonic waveriders, Sci Sin Tech 44 (No. 10) (March 2014) 1114–1122, https://doi.org/10.1360/N092014-00058 (in Chinese).
[14] Tarpley, C., Lewis, M. J., "Stability derivatives for a hypersonic caret-wing waverider," J. Aircraft, Vol. 32, July-Aug. 1995, pp. 795-803. doi: 10.2514/3.46793.
[15] A.C. Jain, J.R. Hayes, Hypersonic pressure, skin-friction, and heat transfer distributions on space vehicles: planar bodies, AIAA J. 42 (No. 10) (Oct. 2004) 2060–2069, https://doi.org/10.2514/1.4102.
[16] U. Goldberg, O. Peroomian, P. Batten, S. Chakravarthy, The k-ε-Rt turbulence closure, Eng. Appl. Comput. Fluid Mech. 3 (No. 2) (2009) 175–183, https://doi.org/10.1080/19942060.2009.11015263.
[17] H. Alkandry, I.D. Boyd, A. Martin, Comparison of transport properties models for flowfield simulations of ablative heat shields, J. Thermophys. Heat Tran. 28 (No. 4) (2014) 569–582, https://doi.org/10.2514/1.T4233.
[18] R.N. Gupta, J.M. Yos, R.A. Thompon, et al., A review of reaction rates and thermodynamic and transport properties for an 11-species air model for chemical and thermal nonequilibrium calculations to 30000K, in: NASA-RP-1232, NASA Langley Research Center, Washington, 1990.
[19] M.J. Wright, D. Bose, G.E. Palmer, E. Levin, Recommended collision integrals for transport property computations Part 1: air species, AIAA J. 43 (No. 12) (2005) 2558–2564, https://doi.org/10.2514/1.16713.
[20] W. Liu, C.A. Zhang, F.M. Wang, Modification of hypersonic waveriders by vorticity-based boundary layer displacement thickness determination method, Aero. Sci. Technol. 75 (Jan) (2018) 200–214, https://doi.org/10.1016/j.ast.2017.12.020.
[21] W. Liu, C.A. Zhang, H.Q. Han, F.M. Wang, Local piston theory with viscous correction and its application, AIAA J. 55 (No. 3) (March 2017) 942–954, https://doi.org/10.2514/1.J055207.
[22] K. Hannemann, S.J. Martinez, S. Karl, et al., Cylinder Shock Layer Density Profiles Measured in High Enthalpy Flows in HEG," *22nd AIAA Aerodynamic Measurement Technology and Ground Testing Conference*, AIAA, June 2002. Paper 2002-2913.
[23] V.B. Betelin, A.G. Kushnirenko, N.N. Smirnov, et al., Numerical investigations of hybrid rocket engines, Acta Astronaut. 144 (2018) 363–370, https://doi.org/10.1016/j.actaastro.2018.01.009.
[24] A.G. Kushnirenko, L.I. Stamov, V.V. Tyurenkova, et al., Three-dimensional numerical modeling of A rocket engine with solid fuel, Acta Astronaut. 181 (2021) 544–551, https://doi.org/10.1016/j.actaastro.2021.01.028.
[25] N.N. Smirnov, V.B. Betelin, V.F. Nikitin, et al., Accumulation of errors in numerical simulations of chemically reacting gas dynamics, Acta Astronaut. 117 (2015) 338–355, https://doi.org/10.1016/j.actaastro.2015.08.013.
[26] J.D. Anderson Jr., Hypersonic and High-Temperature Gas Dynamics, second ed., AIAA, Reston, VA, 2006, pp. 301–305.